Research Article | Vol. 28, No. 21 / 12 October 2020 / Optics Express 31553
Optics EXPRESS

Characterization of space-momentum entangled photons with a time resolving CMOS SPAD array

BRUNO ECKMANN,[1] BÄNZ BESSIRE,[1] MANUEL UNTERNÄHRER,[1] LEONARDO GASPARINI,[2] MATTEO PERENZONI,[2] AND ANDRÉ STEFANOV[1,*]

[1] *Institute of Applied Physics, University of Bern, 3012 Bern, Switzerland*
[2] *Fondazione Bruno Kessler FBK, 38122 Trento, Italy*
[*] *andre.stefanov@iap.unibe.ch*

Abstract: Single-photon avalanche diode arrays can provide both the spatial and temporal information of each detected photon. We present here the characterization of spatially entangled photons with a 32×32 pixel sensor, specifically designed for quantum imaging applications. The sensor is time-tagging each detection event at pixel level with sub-nanosecond accuracy within frames of 50 ns. The spatial correlations between any number of detections in a defined temporal window can thus be directly extracted from the data.The space-momentum entanglement of photon pairs is demonstrated by violating an EPR-type inequality directly from the measured near-field correlations and far-field anti-correlations.

1. Introduction

Quantum states of light are a fundamental tool to implement quantum information processing protocols and quantum metrology methods in the optical domain, such as quantum imaging [1]. They can be described either by discrete variables, the photons, or by continuous fields. Correspondingly measurements of light can be mainly split into two classes: measurements of fields, by homodyne detection for example, and intensity measurements, that correspond fundamentally to photon counting. These are the tools of choice to characterize discrete quantum optical states; for example to measure correlations in quantum states with few photons. An ideal detector should be able to detect the position and time of arrival of all impinging photons. Such universal detectors do not yet exist, but there are various types of single photon sensitive detectors that are each optimized with respect to specific characteristics. Most of the experiments based on correlations between photons are realized with single photon detectors with high temporal resolution but no spatial resolution [2], including photomultipliers, single photon avalanche diodes (SPAD) or superconducting detectors. On the other side, imaging experiments are usually implemented, even at the single photon level, with low noise cameras as EMCCD or scientific CMOS cameras [3,4], that are able to localize single photons among many pixels, but have low temporal resolution. Spatial entanglement in photon pairs has been demonstrated with scanning single pixel detectors [5], EMCCD [6] and commercial gated single photon avalanche array sensors [7]. Correlations between photons from a pair, one detected by a single pixel detector and the other one by an ICCD camera, have also been measured [8,9].

A way to combine high temporal and spatial resolution is fast gating of imaging sensors. However, while gating gives access to short times, the full spatio-temporal correlations of light across a wide temporal range cannot be measured. In addition, gating is well suited for pulsed operations, but a continuous source of correlated photons would ideally be measured with a non-synchronous detector. This is easily implemented with single pixel detectors, that are always ready to trigger, up to their dead-time. However when operating many detectors in parallel, as in detector arrays, the readout mechanism usually requires a frame-based operation. In that

#401260 https://doi.org/10.1364/OE.401260
Journal © 2020 Received 1 Jul 2020; revised 2 Sep 2020; accepted 13 Sep 2020; published 6 Oct 2020

Optics EXPRESS

case, one of the criterion to be optimized is the sensor duty cycle defined by the product of the frame repetition rate of the detector with the duration of each frame. For gated detectors, the requirement to have short gates in order to achieve a good temporal discrimination of correlated photons contradicts the need of long frames to improve the photon collection efficiency. The solution is the ability to time-stamp with high temporal resolution each detection event within a long frame. Combining single photon detectors and external time-stamping electronics can be realized only for a small number of detectors [10]. This cannot, however, be extended to imaging with thousands of pixels without the integration of light sensitive devices with digital electronics, as offered by CMOS technology. Event based high-speed optical cameras have the ability to time-stamp many detection events at a very high rate. Single photon sensitivity can be achieved in combination with an image intensifier, however at the expense of the temporal and spatial resolutions. Correlation between polarization-entangled photon pairs have been demonstrated with such devices [11]. In this work, we demonstrate the capability of a recently developed SPAD array sensor [12–14] to characterize spatial entanglement from spontaneous parametric down-conversion (SPDC) by measuring both, near- and far-field correlations [5,6]. We demonstrate entanglement of the state by testing an Einstein-Podolsky-Rosen (EPR)-type inequality. The direct access to each individual coincidence event allows to estimate the violation of the inequality directly from the measured joint-probabilities, without a priori assumption on the quantum state. In addition, it can be estimated from fitted data, assuming a Gaussian model for the SPDC emission.

In section 2. we recall the quantum state of the photon pairs emitted by SPDC and the expected joint-probability distribution that have to be measured in order to verify their spatial entanglement. Section 3. describes the experimental setup and the processing of the data acquired with the SPAD array, in particular the corrections of the accidental events and crosstalk. The results are presented in section 4., with the different estimations of the violation of the inequality. Finally, in section 5., we introduce figures of merit for the comparison of various sensor technologies in the case of the detection of n-photon correlations in continuous sources of light.

2. Theory of spatial entanglement in SPDC

SPDC is nowadays a common source of entangled photon pairs, where a pump photon of frequency ω_p is annihilated inside a non-linear crystal (NLC) with a non-vanishing second-order susceptibility $\chi^{(2)}$, and two photons with frequencies ω_1 and ω_2 and wave-vectors $\mathbf{k}_1$ and $\mathbf{k}_2$ (historically called *signal* and *idler*) are simultaneously created [15]. Here we consider the case of type-0 quasi-phase-matching in a periodically poled crystal of length L with poling period G and refractive index $n(\omega)$, where all fields have the same polarization [16].

Under the approximation of a monochromatic pump with a frequency ω_{cp}, the envelope of the pump field is given by

$$\mathcal{E}_p^+(\mathbf{q}_p, \omega_p) = 2\pi\mathcal{E}_p^+(\mathbf{q}_p)\delta(\omega_p - \omega_{cp}), \tag{1}$$

where $\mathcal{E}_p^+(\mathbf{q}_p)$ describes the amplitude in momentum space. The quantum state of the generated signal and idler photons is then given by

$$|\Psi\rangle = |0\rangle + \int d\mathbf{q}_1 d\mathbf{q}_2 d\omega_2 \; \Lambda(\mathbf{q}_1, \mathbf{q}_2, \omega_2)\hat{a}^\dagger(\mathbf{q}_1, \omega_{cp} - \omega_2)\hat{a}^\dagger(\mathbf{q}_2, \omega_2)|0\rangle, \tag{2}$$

where $\mathbf{q}_i = (k_{x_i}, k_{y_i})$ is the transverse component of the wave vector $\mathbf{k}_i$ and $|0\rangle$ is the multimode vacuum. The two-photon wave-function, or joint momentum amplitude (JMA) is

$$\begin{aligned}\Lambda(\mathbf{q}_1, \mathbf{q}_2, \omega_2) = &-\frac{4i\epsilon_0\chi^{(2)}Le(\omega_{cp} - \omega_2)e(\omega_2)}{3\hbar\pi(2\pi)^5\, n(\omega_{cp} - \omega_2)n(\omega_2)}\mathcal{E}_p^+(\mathbf{q}_1 + \mathbf{q}_2) \\ &\times \operatorname{sinc}\left(\frac{\Delta k_z L}{2}\right) \exp\left(-i\frac{\Delta k_z L}{2}\right),\end{aligned} \tag{3}$$

Optics EXPRESS

with the phase matching relation

$$\begin{aligned}\Delta k_z =&\sqrt{\left(\frac{\omega_{cp}-\omega_2}{c}n(\omega_{cp}-\omega_2)\right)^2-\mathbf{q}_1^2}+\sqrt{\left(\frac{\omega_2}{c}n(\omega_2)\right)^2-\mathbf{q}_2^2}\\&-\sqrt{\left(\frac{\omega_{cp}}{c}n(\omega_{cp})\right)^2-(\mathbf{q}_1+\mathbf{q}_2)^2}+\frac{2\pi}{G},\end{aligned}\tag{4}$$

and the normalization function

$$e(\omega)=i\sqrt{\frac{\hbar\omega}{2(2\pi)^3\epsilon_0 c}}.\tag{5}$$

We note that the JMA $\Lambda(\mathbf{q}_1,\mathbf{q}_2,\omega_2)$ given by Eq. (3) cannot in general be factorized into functions $\Lambda_i(\mathbf{q}_1,\omega_2)$ and $\Lambda_s(\mathbf{q}_2,\omega_2)$ and thereby the state is entangled. Assuming narrow-band frequency filtering of the down-converted photons and thus only considering the spatial dependency, the JMA factorizes into momentum and frequency parts [17]

$$\Lambda(\mathbf{q}_1,\mathbf{q}_2,\omega_s)=\Lambda(\mathbf{q}_1,\mathbf{q}_2)S(\omega_2).\tag{6}$$

Equivalently, the JMA can be expressed in term of transverse positions $(\boldsymbol{\rho}_1,\boldsymbol{\rho}_2)$ and times (t_1,t_2) through spatial and temporal Fourier transforms $\mathcal{F}$

$$\tilde{\Lambda}(\boldsymbol{\rho}_1,\boldsymbol{\rho}_2)\tilde{S}(\tau)=\mathcal{F}\{\Lambda(\mathbf{q}_1,\mathbf{q}_2)\}\mathcal{F}\{S(\omega_2)\}.\tag{7}$$

In the monochromatic approximation, the temporal part only depends on the time difference $\tau=t_1-t_2$. Coincidence detections measure events around $\tau=0$. Therefore the temporal part of the JMA only accounts for a proportionality factor and thus will be further omitted.

The position $\boldsymbol{\rho}_i=(x_i,y_i)$ and momentum $\hbar\boldsymbol{q}_i=(\hbar k_{x_i},\hbar k_{y_i})$ operators do not commute and therefore a criterion for EPR-type correlations between two systems 1 and 2 (that correspond in our case to the signal and idler photons) can be established [18]. In the SPDC emission, the x and y components are decoupled. We thus consider the one dimensional case with x_i and $p_i=\hbar k_{x_i}$. The results of correlation measurements are therefore described by the joint-probabilities $\mathcal{P}(\boldsymbol{\rho}_1,\boldsymbol{\rho}_2)$ and $\mathcal{P}(\boldsymbol{q}_1,\boldsymbol{q}_2)$, or $\mathcal{P}(x_1,x_2)$ and $\mathcal{P}(p_1,p_2)$ in the 1D case. The minimal inferred variance of (x_1,x_2) is defined by

$$\Delta^2_{min}(x_1|x_2)=\int dx_2\ \mathcal{P}(x_2)\Delta^2(x_1|x_2),\tag{8}$$

where $\Delta^2(x_1|x_2)$ is the variance of the conditional probability $\mathcal{P}(x_1|x_2)$ and $\mathcal{P}(x_2)$ is the marginal probability of system 2. Analogue definitions apply for the variables (p_1,p_2). According to [18], the fulfillment of the following inequality on the product of minimum inferred variances indicates EPR-type correlations, or entanglement

$$\Delta^2_{min}(x_1|x_2)\Delta^2_{min}(p_1|p_2)<\frac{\hbar^2}{4},\tag{9}$$

or expressed as a dimensionless inequality

$$\Delta^2_{min}(x_1|x_2)\Delta^2_{min}(k_{x_1}|k_{x_2})<\frac{1}{4}.\tag{10}$$

Experimentally, the joint-probabilities are derived from correlation measurements that correspond to second-order coherence functions of the electric field. They are given at transverse positions

Optics EXPRESS

$\boldsymbol{\rho}_1$ and $\boldsymbol{\rho}_2$ and times t_1 and t_2 by

$$G^{(2)}(\boldsymbol{\rho}_1, t_1; \boldsymbol{\rho}_2, t_2) = \langle \hat{E}^-(\boldsymbol{\rho}_1, t_1)\hat{E}^-(\boldsymbol{\rho}_2, t_2)\hat{E}^+(\boldsymbol{\rho}_2, t_2)\hat{E}^+(\boldsymbol{\rho}_1, t_1)\Psi\rangle. \tag{11}$$

Correspondingly, in the monochromatic approximation the joint-probability is directly proportional to the second-order coherence function

$$\mathcal{P}(\boldsymbol{\rho}_1, \boldsymbol{\rho}_2) \propto G^{(2)}(\boldsymbol{\rho}_1, \boldsymbol{\rho}_2) \tag{12}$$

and, at the crystal position, is explicitly related to the spatial JMA of the state Eq. (2) by

$$G^{(2)}(\boldsymbol{\rho}_1, \boldsymbol{\rho}_2) \propto \left|\tilde{\Lambda}(\boldsymbol{\rho}_1, \boldsymbol{\rho}_2)\right|^2. \tag{13}$$

In general, the imaging setup from the crystal to the sensor plane determines the field operators that have to be introduced in Eq. (11). In the following, we performed the two types of measurements relevant for inequality (10): near- and far-field imaging.

2.1. Second-order near-field correlations

When imaging the crystal with a magnification M, the correlation function at the image plane using Fourier optics can be expressed as

$$G^{(2)}_{NF}(\boldsymbol{\rho}_1, \boldsymbol{\rho}_2) \propto \left| \int d\mathbf{q}_1 \int d\mathbf{q}_2 \Lambda(\mathbf{q}_1, \mathbf{q}_2) e^{i(\mathbf{q}_1\boldsymbol{\rho}_1 + \mathbf{q}_2\boldsymbol{\rho}_2)/M} \right|^2. \tag{14}$$

This is essentially the Fourier transform of the propagated two-photon JMA.

2.2. Second-order far-field correlations

In a far-field imaging setup at wavelength $\lambda = 2\pi/k$, using a lens of focal length f, the relation between the transverse position at the imaging plane $\boldsymbol{\rho}$ and the transverse momentum $\mathbf{q}$ at the object is

$$\mathbf{q} = \frac{k}{f}\boldsymbol{\rho}. \tag{15}$$

Hence, the second-order correlation function in the far-field reads

$$G^{(2)}_{FF}(\boldsymbol{\rho}_1, \boldsymbol{\rho}_2) \propto \left| \Lambda\left(\frac{k}{f}\boldsymbol{\rho}_1, \frac{k}{f}\boldsymbol{\rho}_2\right) \right|^2. \tag{16}$$

The spatial dependency of the correlation function thus directly reflects the JMA expressed in the momentum space.

3. Experimental evaluation of correlations

The joint-probability distribution that leads to the evaluation of Eq. (10) has to be estimated from the raw correlations acquired with the SPAD array sensor. Ideally it should be estimated directly from the non-processed data, in order to achieve a non-conditional violation of the inequality. However due to the sensor imperfections, such as reduced efficiency, dark counts and crosstalk between pixels, some assumptions have to be introduced to process and correct the raw data. In a second step, the corrected data can be either directly used to numerically evaluate Eq. (10) or, by introducing additional assumptions, fitted with a model of the expected correlations as it is done for instance in [6].

Optics EXPRESS

3.1. Experimental setup

The experimental setup is shown in Fig. 1. A continuous wave (CW) laser (Toptica DL PRO HP 405) with a maximal power output of 30 mW at a wavelength of 405 nm and a spectral bandwidth of 80 MHz serves as the pump. It is slightly focused onto the crystal's center plane Σ_0 by a two-lens system ($f_1 = f_2 = 200$ mm). The beam waist of the pump at this plane is $w_{0x} = 250$ µm in the x direction and and $w_{0y} = 300$ µm in the y direction. Quarter and half-wave plates are used to achieve the desired horizontal polarization in the crystal. A $1 \times 2 \times 12$ mm^3 periodically poled $KTiOPO_4$ (PPKTP) NLC with poling period $G_0 = 3.51043$ µm is embedded into a temperature controlled oven and provides the source for the down-converted photons. The oven is maintained at a temperature of 26.0 °C for an almost collinear phase-matching, that maximizes the photon flux onto the sensor in the far field. The down-converted photons are separated from the pump by a bandpass filter (BP) centered at 810 nm with FWHM 10 nm. About 2 nW of entangled photons are produced, that corresponds to about 4×10^9 photon pairs, or 200 photon per frames of 50 ns. Given the source parameters, waists of the pump beam and the length of the SPDC crystal, we can estimate the minimal inferred standard deviations to be

$$\Delta_{min}(x_1|x_2) = 37.3\ \mu\text{m} \qquad \Delta_{min}(k_{x_1}|k_{x_2}) = 4.0\ \text{mm}^{-1}, \tag{17}$$

$$\Delta_{min}(y_1|y_2) = 37.3\ \mu\text{m} \qquad \Delta_{min}(k_{y_1}|k_{y_2}) = 3.4\ \text{mm}^{-1}, \tag{18}$$

leading to the following violation of the Heisenberg-inferred inequalities

$$V^{(x)}_{min} \equiv \Delta^2_{min}(x_1|x_2)\Delta^2_{min}(k_{x_1}|k_{x_2}) = 2.2 \times 10^{-2} \tag{19}$$

$$V^{(y)}_{min} \equiv \Delta^2_{min}(y_1|y_2)\Delta^2_{min}(k_{y_1}|k_{y_2}) = 1.6 \times 10^{-2}. \tag{20}$$

Two lenses ($f_3 = f_4 = 50$ mm) form a $4f$ imaging system such that the electric field at the plane Σ_{NF} is an exact replica of the field in the crystal at Σ_0. Either the near- or far-field of this plane is then imaged onto the sensor, depending on the selected lens. For near-field, a lens $f_{NF} = 25.4$ mm images the plane Σ_{NF} onto the sensor with a magnification factor $M = 9$. For far-field, a lens $f_{FF} = 150$ mm images the far-field such that the area covered by the sensor corresponds in k-space to ± 36.2 mm^{-1}, as $q = x\frac{k}{f_{FF}}$.

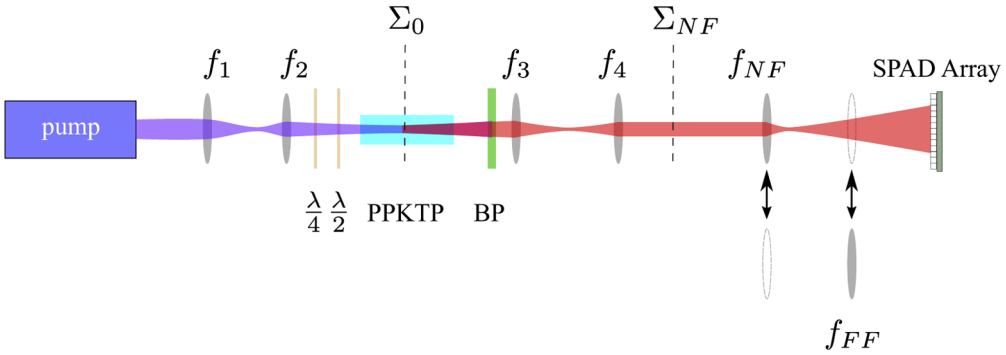

Fig. 1. Experimental setup for spatial correlation measurements. A CW laser at 405 nm is slightly focused by a telescope (f_1 and f_2) and pumps the crystal. The bandpass filter (BP) only transmits the down-converted photons at a central frequency of 810 nm. The 4-f lens configuration (f_3 and f_4) one to one images the crystal center Σ_0 onto the near field plane Σ_{NF}. Further imaging onto the detector array occurs by either a one lens configuration f_{NF} for the near field or a Fourier lens f_{FF} for the far field.

The coincidence detection is performed with a single photon avalanche detector (SPAD) array recently developed [12,13]. It is a fully digital 32×32 pixel sensor array based on CMOS

Optics EXPRESS

technology. The total sensitive area is $1.4 \times 1.4\text{mm}^2$ and the pixel pitch ΔL is 44.64 µm with an overall fill-factor of 19.48 %. A time-to-digital converter (TDC) integrated in each pixel allows for pixel-wise time stamping the first detection event within a frame. The time resolution (time-bin length) of the TDC is 210 ps with a depth of 8 bits, corresponding to an observation time of 255 time-bins or about 50 ns. The mean frame observation rate is about 850 kHz, with peaks up to 1 MHz, which corresponds to a duty cycle of 4.5 %. The total expected photon detection efficiency, when the sensor is active, is 5 % at 400 nm and 0.8 % at 810 nm. The dark count rate per pixel is below 1 kHz at room temperature on average, that correspond to 5×10^{-5} events/frame. The raw data from the sensor's FPGA are transfered to a computer through a USB 3.0 interface and are then post-processed.

3.2. Data processing

The coordinate and time of all detection events within one frame, together with the frame identification number, constitute the acquired raw data. In the following we associate the spatial coordinate $\boldsymbol{\rho}_i = (x_i, y_i)$ with the pixel coordinate $\mathbf{p}_i = (\mathrm{p}_{x_i}, \mathrm{p}_{y_i})$ using $\boldsymbol{\rho}_i = \Delta L \mathbf{p}_i$. An estimation of the raw correlation $G^{(2)}_{raw}(\boldsymbol{\rho}_1, \boldsymbol{\rho}_2)$ between a pair of pixels, or equivalently of $G^{(2)}_{raw}(\mathbf{p}_1, \mathbf{p}_2)$, is obtained by counting all coincidence events between those pixels that occur within a defined temporal window. The histogram of the absolute time differences between all pairs of detection events across the sensor is shown on Fig. 2. While the temporal jitter of each pixel is of the order of 200 ps, in practice temporal shifts across the sensor widen the coincidence peak. In principle, a pixel-wise temporal calibration would allow to narrow the window [13]. Here we define the coincidence window to be ±10 TDC steps (∼ ±2 ns) in order to catch all coincidence events. The obtained histogram is further normalized to a number of coincidences per frame (or alternatively per million of frame, MFrame) [17]. Hence for the data of Fig. 2, 5×10^{-3} true coincidences events per frame are detected within the coincidence window for 3.7×10^{-2} accidental coincidences. The processing of those raw data includes first the subtraction of accidental coincidences, and then a correction step for crosstalk.

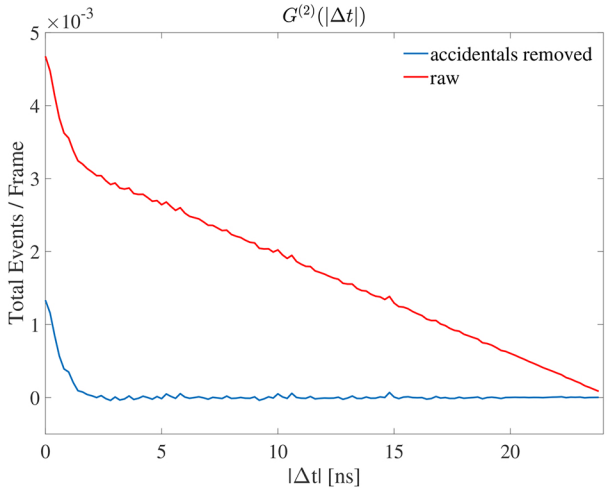

Fig. 2. The temporal second-order correlation $G^{(2)}(|\Delta t|)$ accumulated over all pixels. The raw detection event counts are shown and after removal of uncorrelated accidentals.

Before describing in detail the processing steps, we introduce various representations of the second-order correlation. In a transverse plane it is a function of four variables $G^{(2)}(\mathbf{p}_1, \mathbf{p}_2) = G^{(2)}(\mathrm{p}_{x_1}, \mathrm{p}_{y_1}, \mathrm{p}_{x_2}, \mathrm{p}_{y_2})$. In order to be able to plot a 2D representation of the full correlations, we

Optics EXPRESS

introduce the pixel indices numerating each pixel from 1 . . . 1024

$$\tilde{p}_i = p_{x_i} + 32 \times (p_{y_i} - 1). \tag{21}$$

Fig. 3 shows the full correlation matrix between every pair of pixels after subtraction of accidental events (see section 3.2.1) in the case of far-field measurement. The photon pairs exhibit anti-correlation in their detection positions, that reflects into the ≈ 8 anti-diagonal lines. The nearest neighbors correlations (separated by pixel indexes ±1 and ±32) are affected from crosstalk, forming the four diagonal lines. The exact diagonal cancels, as the sensor cannot measure self-correlations on one pixel.

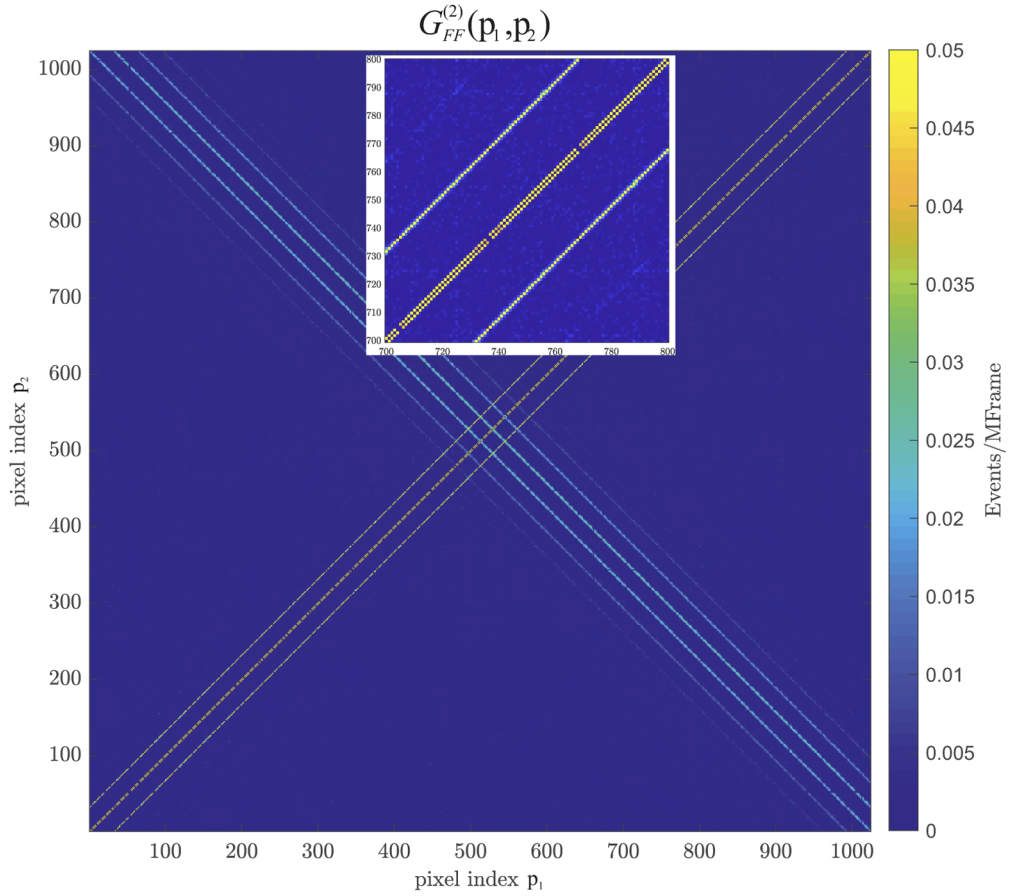

Fig. 3. Full second-order correlations between every pixel pair in the far-field with corrected accidentals. Each pixel is addressed with a linear pixel index $\tilde{p}_i = 1, \ldots, 1024$. The inset shows a close up of the crosstalk correlations appearing along the diagonals.

In order to apply the inequality (10) for only one dimension, the correlation functions are projected onto either the x or y dimension by

$$G^{(2)}(x_1, x_2) = \sum_{y_1} \sum_{y_2} G^{(2)}(x_1, y_1, x_2, y_2), \tag{22}$$

$$G^{(2)}(y_1, y_2) = \sum_{x_1} \sum_{x_2} G^{(2)}(x_1, y_1, x_2, y_2). \tag{23}$$

Optics EXPRESS

Alternatively, one can use the centroid and difference coordinates to project the 4D correlation function on 2D planes defined by fixed values of $\boldsymbol{\rho}_1 + \boldsymbol{\rho}_2$ or $\boldsymbol{\rho}_1 - \boldsymbol{\rho}_2$, respectively. The projected correlation functions read

$$G^{(2)}(\boldsymbol{\rho}_+) = \sum_{\substack{\boldsymbol{\rho}_1,\boldsymbol{\rho}_2 \\ \boldsymbol{\rho}_1+\boldsymbol{\rho}_2=\sqrt{2}\boldsymbol{\rho}_+}} G^{(2)}(\boldsymbol{\rho}_1,\boldsymbol{\rho}_2), \tag{24}$$

$$G^{(2)}(\Delta x,\Delta y) = G^{(2)}(\boldsymbol{\rho}_-) = \sum_{\substack{\boldsymbol{\rho}_1,\boldsymbol{\rho}_2 \\ \boldsymbol{\rho}_1-\boldsymbol{\rho}_2=\sqrt{2}\boldsymbol{\rho}_-}} G^{(2)}(\boldsymbol{\rho}_1,\boldsymbol{\rho}_2). \tag{25}$$

3.2.1. Removing accidentals

Accidental coincidences are coincidence events that occur in the defined coincidence window but are neither temporally nor spatially correlated. They stem from detections triggered by background light, dark counts, and mostly from SPDC photons that do not belong to the same photon pair. The total measured raw correlation signal is thus given by the sum of the accidental coincidences and the true temporal coincidences (as due to photons from a pair)

$$G^{(2)}_{raw}(\boldsymbol{\rho}_1,\boldsymbol{\rho}_2) = G^{(2)}_{pairs}(\boldsymbol{\rho}_1,\boldsymbol{\rho}_2) + G^{(2)}_{acc}(\boldsymbol{\rho}_1,\boldsymbol{\rho}_2) \tag{26}$$

These accidental events contribute significantly to the raw signal as we can observe on Fig. 4(a). They can be however estimated and corrected for, either by measuring the coincidence signal in a shifted time window or by using the fact that uncorrelated light obeys

$$G^{(2)}_{acc}(\boldsymbol{\rho}_1,\boldsymbol{\rho}_2) \propto G^{(1)}(\boldsymbol{\rho}_1)G^{(1)}(\boldsymbol{\rho}_2), \tag{27}$$

where $G^{(1)}(\boldsymbol{\rho})$ is the first-order correlation function, the intensity. The proportionality factor depends on the ratio of the coincidence window length and the frame length. A direct way to estimate it is to compare event rates in $G^{(2)}(\boldsymbol{\rho}_1,\boldsymbol{\rho}_2)$ and $G^{(1)}(\boldsymbol{\rho}_1)G^{(1)}(\boldsymbol{\rho}_2)$ for pixels where no correlations are expected. Figure 4 shows the raw (a) and corrected data after removing accidental coincidences (b). The anti-correlations from the photon pairs are clearly visible, but also correlations due to crosstalk, that are further removed in Fig. 4(c) (see below).

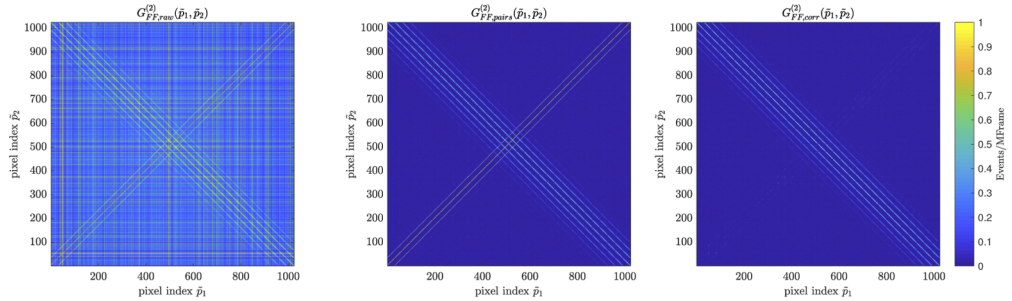

(a) (b) (c)

Fig. 4. Second-order far-field correlations. Measured raw data (a), after removing accidentals (b) and after crosstalk correction (c)

3.2.2. Crosstalk corrections

A single detection event, triggered by a dark count or a photon, can trigger nearby pixels. This leads to undesirable detection events that are an artifact intrinsic to the detector. The physical

Optics EXPRESS

process behind optical crosstalk are photons, created by the charge avalanche of the first triggering SPAD. These photons may reach and trigger neighboring pixels in a very short time-scale. Crosstalk is especially undesired in the near-field correlations, as it overlays the real signal. The crosstalk probability should be estimated for every pixel pair. However, as a first approximation, we assume it to only depend on the distance between two pixels. Thus an average crosstalk value over all pixels can be extracted from the projected correlation function in the far-field $G^{(2)}_{FF}(\Delta x, \Delta y)$, as in that case only anti-correlations are expected. Hence, the mean probability that a pixel at distance $(\Delta x, \Delta y)$ is triggered from crosstalk is given by

$$P_{xtalk}(\Delta x, \Delta y) = \frac{1}{2} \frac{G^{(2)}_{FF}(\Delta x, \Delta y)}{\sum_x \sum_y G^{(1)}_{FF}(x, y)}, \tag{28}$$

where the sum over $G^{(1)}_{FF}$ normalizes with the total number of counts. Any second-order correlation measurements $G^{(2)}_{pairs}$ can then be corrected [19] according to

$$\begin{aligned} G^{(2)}_{corr}(x_1, y_1, x_2, y_2) =& G^{(2)}_{pairs}(x_1, y_1, x_2, y_2) \\ &- P_{xtalk}(x_2 - x_1, y_2 - y_1) G^{(1)}(x_1, y_1) \\ &- P_{xtalk}(x_1 - x_2, y_1 - y_2) G^{(1)}(x_2, y_2), \end{aligned} \tag{29}$$

Figure 5 shows the anti-correlation peak of the far-field signal (a) with corresponding crosstalk probability map (b) estimated from Eq. (28), which is point-symmetric with respect to $(\Delta x, \Delta y) = (0, 0)$. We notice an asymmetry between the vertical and horizontal crosstalk, due to the geometry of the sensor and that is compatible with measurements realized with classical pulsed light [13].

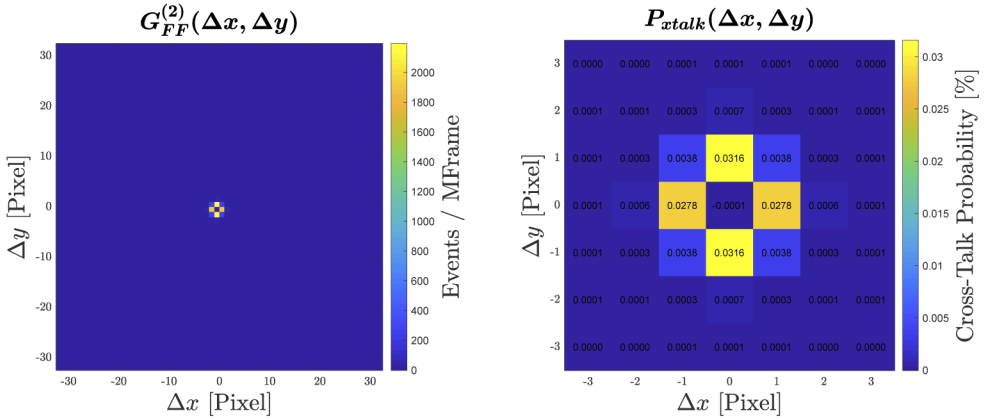

(a) (b)

Fig. 5. (a) Correlation peak due to crosstalk of the second-order correlation measurement in the far-field. (b) Crosstalk probability extracted from the correlation peak. The pixel at $(\Delta x, \Delta y) = 0$ is the emitter of the crosstalk.

4. Measurement results

The full correlation map for far-field measurements is shown on Fig. 4. The same data can then be represented in the other coordinates previously introduced. Figure 6 shows the anti-correlation (a) and correlation (b) peaks in the far-field after crosstalk removal. As far-field measurements map the momentum space onto the sensor, the plots are labeled with the coordinates $\mathbf{q}_+$ and $\mathbf{q}_-$,

Optics EXPRESS

but still in units of pixel. We clearly observe the presence of an anti-correlation peak and the almost disappearance of the correlation peak.

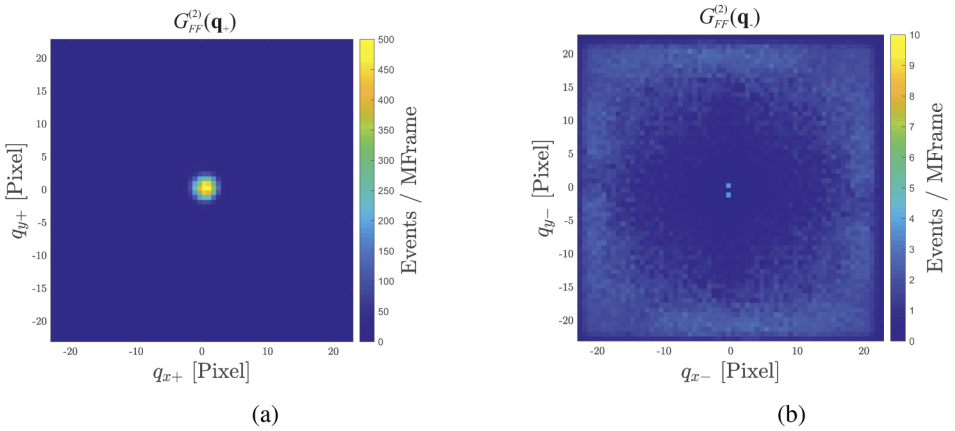

(a) (b)

Fig. 6. Anti-correlation (a) and correlation (b) peaks of the second-order far-field correlation after removing crosstalk.

The same processing can be applied for the near-field measurements. The full correlation matrix is shown in Fig. 7 without (a) and with (b) crosstalk correction. We observe that the crosstalk along the diagonal overlays the actual signal, even after correction. As the crosstalk contribution is of the same order as the signal, its correction is very sensitive to the estimation of the crosstalk probabilities. A calibration at the pixel level would allow for a full correction in future experiments. This is why in the present work, the next neighbor correlations will not be taken into account for the quantitative estimation of the correlations. The partial suppression of the crosstalk can also be seen in the correlation peaks of Fig. 7(c) and (d), where the bright central peak is due to crosstalk, while the broad peak indicates correlation between photons. The magnification factor of the optical system has been chosen in order to obtain a correlation peak broader than the crosstalk.

Figure 8 shows the second-order correlations projected onto the x and y coordinates after removing crosstalk in the far- (a) and (c) and near-field (b) and (d). The correlations affected by crosstalk are set to zero on those plots. The anti-correlations in momentum and correlations in position space are clearly visible. Those data are further used to evaluate the EPR-type inequality.

While the identification of EPR-type correlations should be ideally done on the raw correlations $G^{(2)}_{raw}(\mathbf{p}_1, \mathbf{p}_2)$, usually some additional assumptions are applied to correct for the imperfections of the sensor. Because the detector sensitivity is limited at the SPDC photons wavelength, the accidental and crosstalk are not negligible and have to be corrected as described. In a second step, the corrected data from the second-order correlations in the near-field $G^{(2)}_{NF,corr}(\mathbf{p}_1, \mathbf{p}_2)$ and far-field $G^{(2)}_{FF,corr}(\mathbf{p}_1, \mathbf{p}_2)$ can be either directly numerically evaluated, or, introducing further assumption, fitted with a model of the SPDC emission. The results of the various evaluations are summarized in Table 1. The uncertainties are derived from the confidence intervals of the fits from which probability distributions were obtained.

4.1. Numerical evaluation of the EPR inequality

We present in detail the numerical evaluation for the x coordinates, i.e. $G^{(2)}(x_1, x_2)$ and $G^{(2)}(q_{x_1}, q_{x_2})$. The treatment for the y coordinate is identical.

Optics EXPRESS

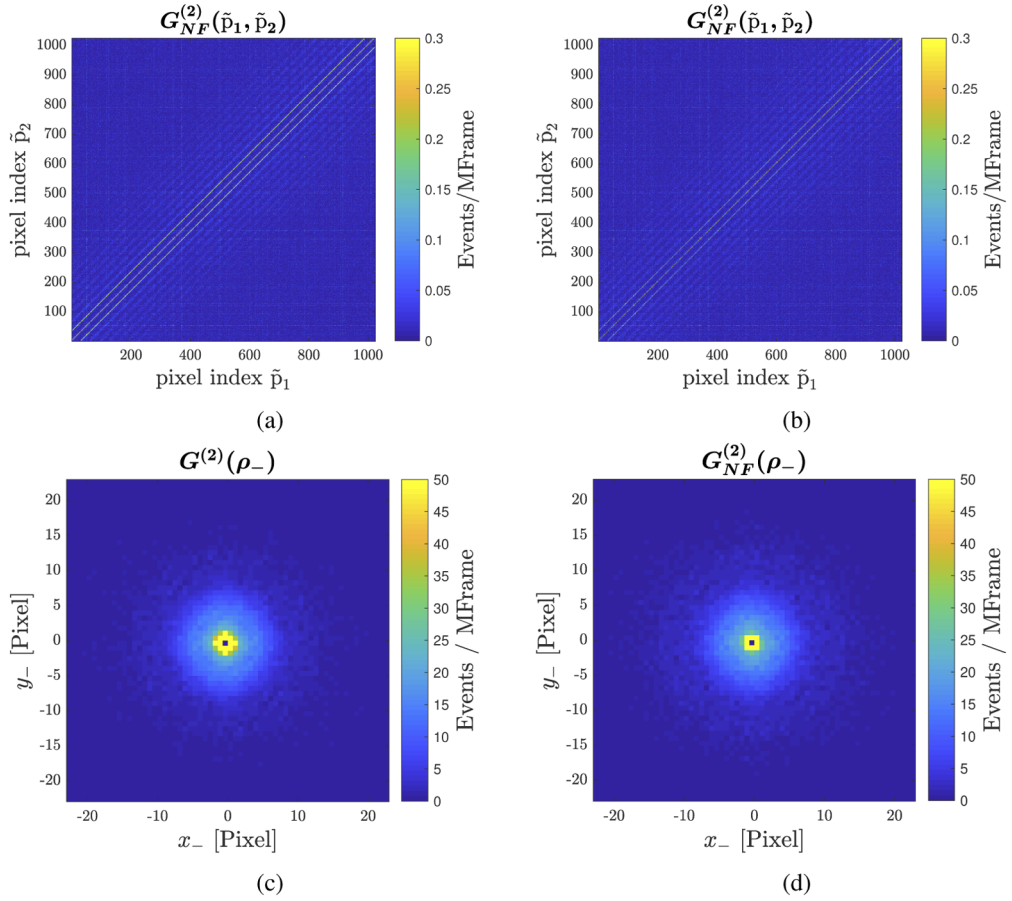

Fig. 7. Second-order near-field correlation with accidentals removed, (a) full correlation matrix and (c) correlation peak. After crosstalk correction, (b) full correlation matrix and correlation peak (d).

Table 1. Results of the evaluation of the conditional variances

	$\Delta_{min}(q_{x1}\|q_{x2})$ /mm^{-1}	$\Delta_{min}(q_{y1}\|q_{y2})$ /mm^{-1}	$\Delta_{min}(x_1\|x_2)$ /µm^{-1}	$\Delta_{min}(y_1\|y_2)$ /µm^{-1}	$V^{(x)}_{min}$ $\times 10^{-2}$	$V^{(y)}_{min}$ $\times 10^{-2}$
numerical	6.3	6.6	37.2	36.2	5.5	5.8
1D fit	3.9	4.1	32.8	30.5	1.6	1.5
2D fit	3.90(3)	4.10(5)	34.4(13)	31.1(9)	1.8(2)	1.6(2)
correlation peak	3.82(5)	3.95(5)	34.3(13)	30.3(11)	1.7(2)	1.4(2)
expected	4.0	3.4	37.3	37.3	2.2	1.6

Optics EXPRESS

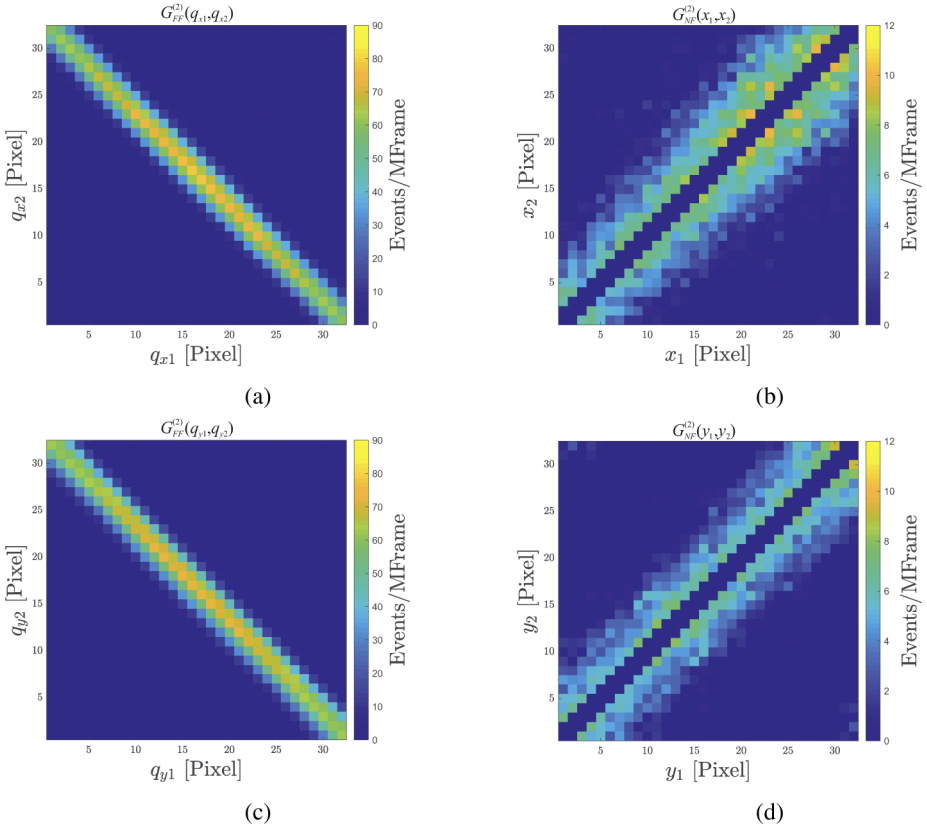

Fig. 8. Second-order correlations in the far-field (a,c) and near-field (b, d) for the x (a,b) and y (c,d) coordinates.

The conditional and unconditional probability density functions are estimated from the corrected experimental data

$$\mathcal{P}(x_1|x_2) = \frac{G^{(2)}_{NF,corr}(x_1|x_2)}{\sum_{x_1} G^{(2)}_{NF,corr}(x_1|x_2)}, \tag{30}$$

$$\mathcal{P}(q_{x_1}|q_{x_2}) = \frac{G^{(2)}_{FF,corr}(q_{x_1}|q_{x_2})}{\sum_{q_{x_1}} G^{(2)}_{FF,corr}(q_{x1}|q_{x_2})}, \tag{31}$$

$$\mathcal{P}(x_2) = \frac{\sum_{x_1} G^{(2)}_{NF,corr}(x_1,x_2)}{\sum_{x_1}\sum_{x_2} G^{(2)}_{NF,corr}(x_1,x_2)}, \tag{32}$$

$$\mathcal{P}(q_{x_2}) = \frac{\sum_{q_{x_1}} G^{(2)}_{FF,corr}(q_{x_1},q_{x_2})}{\sum_{q_{x_1}}\sum_{q_{x_2}} G^{(2)}_{FF,corr}(q_{x_1},q_{x_2})}. \tag{33}$$

Examples of experimentally obtained probability distributions are shown on Fig. 9. Next, the expectation values are given by

$$\mu_{x1} = \sum_{x_1} x_1\, \mathcal{P}(x_1|x_2), \tag{34}$$

Optics EXPRESS

$$\mu_{q_{x1}} = \sum_{q_{x_1}} q_{x_1}\, \mathcal{P}(q_{x_1}|q_{x_2}), \tag{35}$$

and the conditional variances are

$$\Delta^2(x_1|x_2) = \sum_{x_1} (x_1 - \mu_{x1})^2\, \mathcal{P}(x_1|x_2), \tag{36}$$

$$\Delta^2(q_{x_1}|q_{x_2}) = \sum_{q_{x_1}} (q_{x_1} - \mu_{q_{x1}})^2\, \mathcal{P}(q_{x_1}|q_{x_2}). \tag{37}$$

Finally, the minimum inferred variances are computed by

$$\Delta^2_{min}(x_1|x_2) = \sum_{x_2} \mathcal{P}(x_2)\, \Delta^2(x_1|x_2), \tag{38}$$

$$\Delta^2_{min}(q_{x_1}|q_{x_2}) = \sum_{q_{x_2}} \mathcal{P}(q_{x_2})\, \Delta^2(q_{x_1}|q_{x_2}). \tag{39}$$

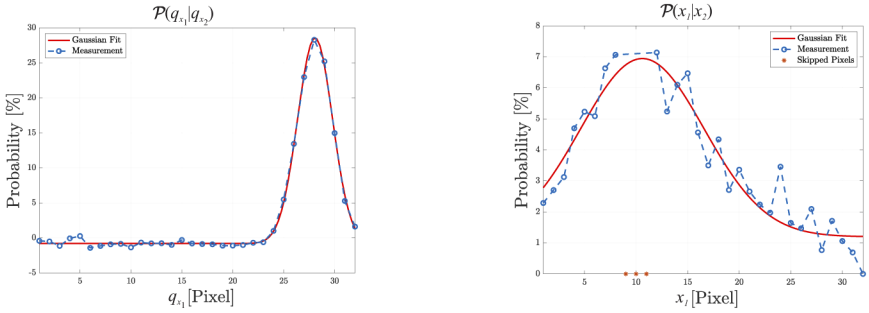

(a) (b)

Fig. 9. Example of measured conditional probabilities for the x variable in the far-field $\mathcal{P}(q_{x_1}|q_{x_2})$ (a) and near-field $\mathcal{P}(x_1|x_2)$ (b). The variance is either extracted numerically or using a Gaussian fit (continuous red line). The pixels affected from crosstalk are skipped (indicated by the red asterisks)

The EPR-type correlations are identified by violating the inequality

$$V^{(x)}_{min} \equiv \Delta^2_{min}(x_1|x_2)\Delta^2_{min}(q_{x_1}|q_{x_2}) > \frac{1}{4}. \tag{40}$$

The same procedure is applied for the y coordinate and the result is denoted as

$$V^{(y)}_{min} \equiv \Delta^2_{min}(y_1|y_2) \times \Delta^2_{min}(q_{y_1}|q_{y_2}) > \frac{1}{4}. \tag{41}$$

The direct numerical evaluation of V_{min} from the corrected measured data is sensitive to the noise of the experiment (mainly shot-noise) but also to the accidental and crosstalk corrections. The measured conditional probability distributions take non-zero values even far away from their expected peak value, as can be seen in Fig. 9. This effect shifts the expectation value $\mu_{x_1,q_{x1}}$ away from the true one and also increases the conditional variances. Setting to zero the pixels affected by crosstalk in the near-field correlations increases the variance of the conditional probability distributions. As a consequence, the numerically determined values of V_{min} given in the first line of Table 1 are overestimated and the violation of the inequality is weaker. While the value V_{min} cannot be used anymore to quantitatively determine the amount of entanglement, it can provide an upper bound on the violation. And therefore, this could not lead to a violation of the inequality with non-entangled light.

Optics EXPRESS

4.2. 1D Gaussian fitting

An alternative approach to direct numerical evaluation is to constrain the data into a set of "reasonable" data, compatible with the expected characteristics of the light source. The shape of the JMA from SPDC emission can be, in some conditions, approximated by Gaussian functions. Therefore $\mathcal{P}(q_{x_2})$, $\mathcal{P}(x_2)$, $\mathcal{P}(q_{x_1}|q_{x_2})$ and $\mathcal{P}(x_1|x_2)$ can be estimated by fitting the data with Gaussian functions. Figures 9 and 10 show examples of fitted data. One can then extract the variances directly from these fitted probability density functions and calculate the EPR-criterion according to the definition of Eqs. (8) and (10). The results are shown in the second line of Table 1 and are in agreement with the expected values derived from the experimental parameters.

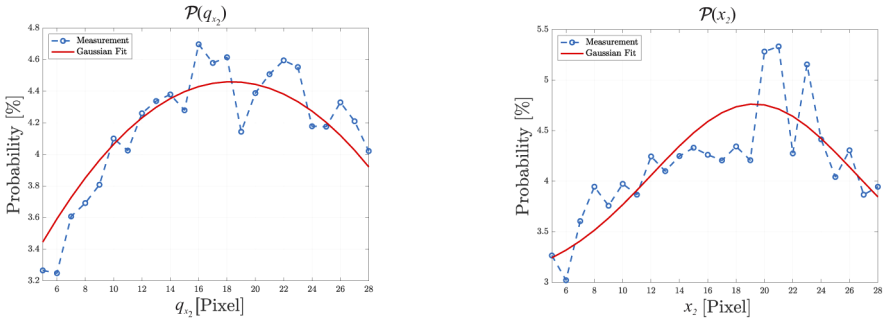

(a) (b)

Fig. 10. Example of measured unconditional probabilities for the x variable in the far-field (a) and near-field (b).

4.3. 2D Gaussian fitting

Instead of fitting multiple Gaussians by slicing the data sets $G^{(2)}$, one can also directly fit $G^{(2)}_{NF,corr}(x_1, x_2)$ and $G^{(2)}_{FF,corr}(q_{x_1}, q_{x_2})$ with 2D Gaussian functions (and similarly for y), as shown on Fig. 11. It is to be observed that we only assume the correlations to be well-approximated by 2D Gaussians with variances $\Delta^2_{x+,x-}$ and $\Delta^2_{qy+,qx-}$ as fitting parameters, but we don't impose the quantum state to follow the double Gaussian model [20]. The conditional variances are then related to the fitting parameters by [21]

$$\Delta^2(x_1|x_2) = \frac{2\Delta^2_{x+}\Delta^2_{x-}}{\Delta^2_{x+} + \Delta^2_{x-}}, \tag{42}$$

$$\Delta^2(q_{x1}|q_{x2}) = \frac{2\Delta^2_{qx+}\Delta^2_{qx-}}{\Delta^2_{qx+} + \Delta^2_{qx-}}. \tag{43}$$

The uncertainties on the values of V_{min} can then be derived from the fits confidence intervals.

4.4. (Anti-) Correlation peaks

Finally, a quick way to estimate the strength of the (anti-) correlations is to consider the projections onto x and y of the (anti-) correlation peaks $G^{(2)}_{FF}(\mathbf{q}_+)$ and $G^{(2)}_{NF}(\boldsymbol{\rho}_-)$ that are shown on Fig. 12. The width of the fitted Gaussian are respectively σ_{x+}, σ_{y+} and $\sigma_{qx+}, \sigma_{qy+}$. They can be related to the conditional variances under the assumption that the correlations, respectively anti-correlations, appear only along the $-$ and $+$ coordinates. Equivalently, the correlations in the near-field are assumed to be expanded very far along the $+$ coordinate (i.e. $\sigma_{x+}, \sigma_{y+} \to \infty$) and similarly in the far-field for the $-$ coordinate ($\sigma_{qx+}, \sigma_{qy+} \to \infty$). Graphically in Fig. 8, the diagonals (b and d)

Optics EXPRESS

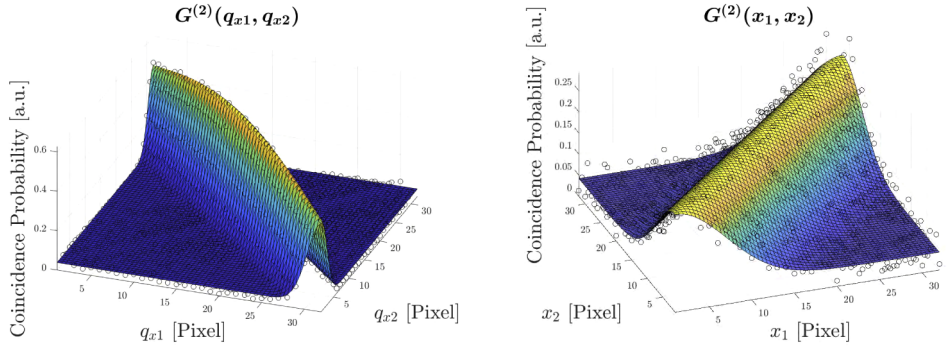

(a) (b)

Fig. 11. The second-order correlations in the far-field (a) and near-field (b) are directly fitted with 2D Gaussian distributions and the variances are extracted from the fits.

and anti-diagonals (b and d) would thus extend to infinity. The conditional variances are then related to the width of the peaks $G^{(2)}(x_-)$ and $G^{(2)}(q_{x+})$ by

$$\Delta(x_1|x_2) \approx \sqrt{2}\sigma_{x-}, \tag{44}$$

$$\Delta(q_{x1}|q_{x2}) \approx \sqrt{2}\sigma_{qx+} \tag{45}$$

and similarly for the y coordinate.

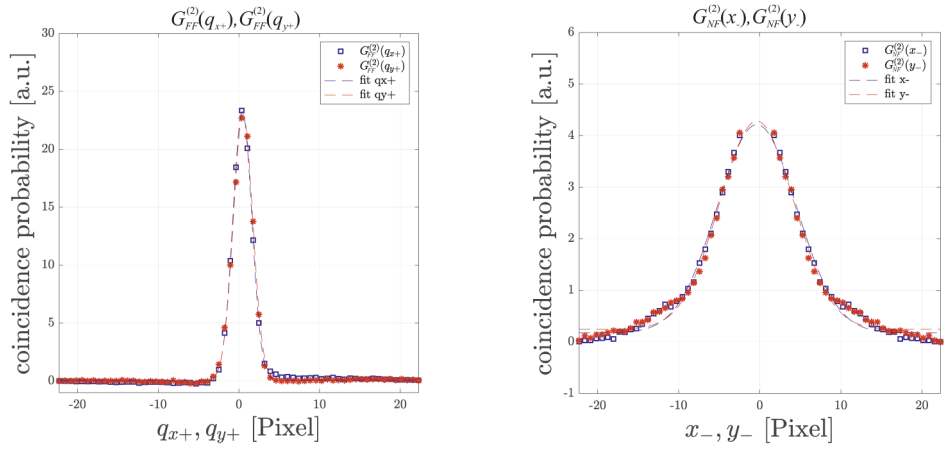

(a) (b)

Fig. 12. Anti-correlations peaks (a) of the second-order correlations in the far-field and correlation peaks (b) from near-field measurements alon x and y directions.

5. Sensors comparison

The previous results show the capacity of SPAD array sensors to detect spatio-temporal coincidences between correlated photon pairs. Hence they provide an alternative technology to ICCD and EMCCD cameras. Comparing different technologies is strongly dependent on the targeted applications. This is why we introduce here figures of merit for selected applications, in order to infer the potential of various sensors. For this purpose we estimate the relative

Optics EXPRESS

effective efficiencies for detecting coincidences, including PDE and duty cycle, for the following detectors: the SPAD array used in this work, a commercial gated SPAD array (MPD SPC[3]), a state-of-the-art ICCD (Andor iStar sCMOS 18* -A3) in full frame or binning modes and high efficiency scanning superconductor single photon detectors (Single Quantum EOS).

We specifically consider the detection of spatio-temporal correlations between n photons emitted from a continuous source of light and we assume a regime of sparse photon detections. The first relevant criteria are the spatial and temporal resolutions. The spatial resolution is determined by the number of pixel N_p. The size of the pixels, or pixel pitch Δp, is here of secondary importance, as the pixel can be fit to arbitrary dimensions by optical magnification (within the restrictions of the optical setup). The temporal resolution is determined by the smallest accessible time-bin Δt, usually given by the detector jitter or the gating time. The number of accessible time-bins is N_t. In contrary to the spatial resolution, the temporal resolution cannot be changed by a stationary linear optical setup. For single (or few pixel detectors), spatial scanning is required, while for gated detectors, temporal scanning is needed. In general, sensors with both spatial and temporal resolution have access to a pixelized volume of space-time of size $N_{st} = N_p \times N_t$, the spatio-temporal resolution. The measurements are repeated at a frame rate ν and each frame gives access to the volume N_{st}. An important additional parameter is the photon detection efficiency PDE including fill factor. The PDE is wavelength dependent, but we only consider the peak PDE across the spectral range. In order to concentrate on the fundamental limitations of different technologies, other characteristics, as noise or crosstalk will not be taken into account in the following estimations. Also we assume a negligible time for the scanning, in order to investigate the intrinsic limitation of the sensors only.

The accessible volume N_{st} is a subset of the total space-time volume of interest that has to be measured, and thus both, spatial and temporal scanning may be required in general. The acquisition time is hence inversely proportional to N_{st} or to an equivalent quantity for high-order correlations.

5.1. Single photon detection

At first we address the problem of building the spatio-temporal histogram of single photon detection $N(\vec{r}, t)$ that corresponds to the intensity distribution $I(\vec{r}, t)$, or in other terms the first order correlation function of the field $\langle \hat{E}^-(\vec{r}, t)\hat{E}^+(\vec{r}, t)\rangle$. This is the case for wide-field LIDAR or fluorescence lifetime imaging microscopy for instance.

In order to compare various detectors we estimate the time needed to scan through a targeted space-time volume $N_{st}^{target} = N_p^{target} N_t^{target}$, defined by a spatial resolution of N_p^{target} and a temporal resolution, in the nanosecond range, of N_t^{target} time-bins. The time required to scan this volume is hence proportional to $N_{st}^{target}/N_{st}/\nu$, or furthermore, by taking into account the PDE to $N_{st}^{target}/N_{st}/\nu/PDE$. Thus, two figures of merit are relevant for spatio-temporal single photon detection, a quantity proportional to the acquisition time

$$M_1 = \frac{1}{N_{st}\nu PDE} \tag{46}$$

that should be minimal and Δt that defines the smallest detectable time interval.

5.2. n photons in coincidence

We extend the previous reasoning to the case where n photons are expected to reach the sensor simultaneously (within a time window smaller than the sensor's temporal resolution). The relevant events are therefore given by n spatial positions and one time coordinate only. This reflects a n-order correlation function $\langle \hat{E}^-(\vec{r}_1, t)\cdots\hat{E}^-(\vec{r}_n, t)\hat{E}^+(\vec{r}_n, t)\cdots\hat{E}^+(\vec{r}_1, t)\rangle$. Here, the targeted volume is given by $N_{st}^{target} = (N_p^{target})^n N_t^{target}$ and the accessible volume is $N_{st} = (N_p)^n N_t$.

Optics EXPRESS

Hence the figures of merit are

$$M_n^* = \frac{1}{(N_p PDE)^n N_t \nu} \tag{47}$$

and Δt.

5.3. n photons at arbitrary times

In the most general case, any possible n-fold coincidence between any position and time, should be registered. This is formaly given by the full nth order correlation function

$$G^n\left(\vec{r}_1, t_1, \ldots, \vec{r}_n, t_n\right) = \langle \hat{E}^-(\vec{r}_1, t_1) \cdots \hat{E}^-(\vec{r}_n, t_n) \hat{E}^+(\vec{r}_n, t_n) \cdots \hat{E}^+(\vec{r}_1, t_1) \rangle. \tag{48}$$

The figures of merit are here

$$M_n = \frac{1}{(N_{st} PDE)^n \nu} \tag{49}$$

and Δt.

Table 2 shows the characteristics of the selected sensors together with the estimated figures of merit for one-photon detection (M_1), two-photon detection at arbitrary times (M_2), two photons in coincidence (M_2^*) and three photons at arbitrary times (M_3). The values are normalized to the values for the SPAD used in the present work that are $M_1^0 = 5.7 \times 10^{-11}, M_2^0 = 2.8 \times 10^{-15}, M_2^{0*} = 7.3 \times 10^{-13}$ and $M_3^0 = 1.4 \times 10^{-19}$. Hence they are proportional to the ratio of acquisition times and therefore smaller is better.

Table 2. Figures of merit of selected single photon sensors.

Sensor	N_p	N_t	ν/Hz	Δt/ns	PDE/%	M_1	M_2	M_2^*	M_3
This work, SPAD	32×32	256	10^6	0.21	8	1	1	1	1
ICCD, full	2560×2160	1	50	2	40	152	1.4	6×10^{-3}	0.01
ICCD, binning	512×512	1	4008	2	40	788	158	0.6	32
Gated SPAD array	64×32	1	96000	1.5	1.5	5430	3×10^6	1×10^4	2×10^9
Single pixel	1	833	8×10^7	0.015	90	0.3	8	25	219

We can observe that SPAD arrays and single pixel detector trade the high number of pixels of ICCD for high acquisition rates. In all the cases, the present SPAD array is much faster than a gated SPAD, thanks to its higher speed and high number of time-bins, while offering a higher temporal resolution. It also competes quite favorably with scanning single photon detectors, that are of advantage only when very high temporal resolution is required. The comparison with ICCD is less clear. For high spatial resolution, the high number of pixels of the ICCD gives it a clear advantage to measure higher order correlation measurements. For moderate spatial resolution however, the present sensor competes favorably, thanks to its high space-time volume N_{st}.

6. Conclusion

In this work we exploit the capacity of a recently developed 32x32 pixel CMOS SPAD array sensor to time-tag each individual photon with high temporal resolution. This allows us to measure the emission of spatially entangled photon pairs from SPDC in the near- and far-field. Anti-correlations in the far-field and correlations in the near-field are observed. From the experimentally measured probability distributions, the violation of an EPR-type inequality is demonstrated. Interestingly the inequality is violated even without fitting the data with a specific model. When assuming Gaussian shape for the probability distributions, the obtained value for the variances are in good agreement with the expected ones derived from the parameters of

Optics EXPRESS

the photon source. Those results demonstrate the ability of CMOS SPAD arrays to effectively measure simultaneously spatial and temporal correlations between photons. Estimated figures of merit show that SPAD arrays compare favorably with other technologies. Future developments will aim at increasing the number of pixels on the one side, and at achieving higher acquisition speed, for instance by event-based technology. SPAD arrays then could become an effective tool for practical implementations of quantum imaging schemes.

Funding

Horizon 2020 Framework Programme (project SUPERTWIN 686731 and the Research and Innovation Programme 852045).

Disclosures

The authors declare no conflicts of interest.

References

1. M. Genovese, "Real applications of quantum imaging," J. Opt. **18**(7), 073002 (2016).
2. M. D. Eisaman, J. Fan, A. Migdall, and S. V. Polyakov, "Invited Review Article: Single-photon sources and detectors," Rev. Sci. Instrum. **82**(7), 071101 (2011).
3. H. K. V. Lotsch, W. T. Rhodes, E. B. A. Adibi, T. Asakura, T. W. Hänsch, T. Kamiya, F. Krausz, B. Monemar, H. Venghaus, H. Weber, H. Weinfurter, and W. T. Rhodes, *Single-Photon Imaging* (Springer, 2011).
4. P.-A. Moreau, E. Toninelli, T. Gregory, and M. J. Padgett, "Imaging with quantum states of light," Nat. Rev. Phys. **1**(6), 367–380 (2019).
5. J. C. Howell, R. S. Bennink, S. J. Bentley, and R. W. Boyd, "Realization of the Einstein-Podolsky-Rosen Paradox Using Momentum- and Position-Entangled Photons from Spontaneous Parametric Down Conversion," Phys. Rev. Lett. **92**(21), 210403 (2004).
6. M. Edgar, D. Tasca, F. Izdebski, R. Warburton, J. Leach, M. Agnew, G. Buller, R. Boyd, and M. Padgett, "Imaging high-dimensional spatial entanglement with a camera," Nat. Commun. **3**(1), 984 (2012).
7. B. Ndagano, H. Defienne, A. Lyons, I. Starshynov, F. Villa, S. Tisa, and D. Faccio, "Imaging entanglement correlations with a single-photon avalanche diode camera," ArXiv p. 2001.03997 (2020).
8. R. S. Aspden, D. S. Tasca, R. W. Boyd, and M. J. Padgett, "EPR-based ghost imaging using a single-photon-sensitive camera," New J. Phys. **15**(7), 073032 (2013).
9. R. Fickler, M. Krenn, R. Lapkiewicz, S. Ramelow, and A. Zeilinger, "Real-Time Imaging of Quantum Entanglement," Sci. Rep. **3**(1), 1914 (2013).
10. R. Tenne, U. Rossman, B. Rephael, Y. Israel, A. Krupinski-Ptaszek, R. Lapkiewicz, Y. Silberberg, and D. Oron, "Super-resolution enhancement by quantum image scanning microscopy," Nat. Photonics **13**(2), 116–122 (2019).
11. C. Ianzano, P. Svihra, M. Flament, A. Hardy, G. Cui, A. Nomerotski, and E. Figueroa, "Fast camera spatial characterization of photonic polarization entanglement," Sci. Rep. **10**(1), 6181 (2020).
12. L. Gasparini, M. Zarghami, H. Xu, L. Parmesan, M. M. Garcia, M. Unternahrer, B. Bessire, A. Stefanov, D. Stoppa, and M. Perenzoni, "A 32×32-pixel time-resolved single-photon image sensor with 44.64μm pitch and 19.48% fill-factor with on-chip row/frame skipping features reaching 800kHz observation rate for quantum physics applications," in *2018 IEEE International Solid - State Circuits Conference - (ISSCC)*, (IEEE, 2018), pp. 98–100.
13. M. Zarghami, L. Gasparini, L. Parmesan, M. Moreno-Garcia, A. Stefanov, B. Bessire, M. Unternahrer, and M. Perenzoni, "A 32x 32-Pixel CMOS Imager for Quantum Optics With Per-SPAD TDC, 19.48% Fill-Factor in a 44.64-μm Pitch Reaching 1-MHz Observation Rate," IEEE J. Solid-State Circuits **55**(10), 2819–2830 (2020).
14. M. Unternährer, B. Bessire, L. Gasparini, M. Perenzoni, and A. Stefanov, "Super-resolution quantum imaging at the Heisenberg limit," Optica **5**(9), 1150 (2018).
15. C. Couteau, "Spontaneous parametric down-conversion," Contemp. Phys. **59**(3), 291–304 (2018).
16. S. Lerch, B. Bessire, C. Bernhard, T. Feurer, and A. Stefanov, "Tuning curve of type-0 spontaneous parametric down-conversion," J. Opt. Soc. Am. B **30**(4), 953 (2013).
17. M. Unternährer, "On Quantum Imaging with Time-Resolving Detector Arrays," Phd thesis, University of Bern (2018).
18. M. D. Reid, P. D. Drummond, W. P. Bowen, E. G. Cavalcanti, P. K. Lam, H. a. Bachor, U. L. Andersen, and G. Leuchs, "Colloquium : The Einstein-Podolsky-Rosen paradox: From concepts to applications," Rev. Mod. Phys. **81**(4), 1727–1751 (2009).
19. G. Lubin, R. Tenne, I. Michel Antolovic, E. Charbon, C. Bruschini, and D. Oron, "Quantum correlation measurement with single photon avalanche diode arrays," Opt. Express **27**(23), 32863 (2019).
20. M. V. Fedorov, Y. M. Mikhailova, and P. a. Volkov, "Gaussian modelling and Schmidt modes of SPDC biphoton states," J. Phys. B: At., Mol. Opt. Phys. **42**(17), 175503 (2009).

Optics EXPRESS

21. J. Schneeloch and J. C. Howell, "Introduction to the transverse spatial correlations in spontaneous parametric down-conversion through the biphoton birth zone," J. Opt. **18**(5), 053501 (2016).